

Thiophene Based Self-Doped Conducting Polymers as Cathode for Aqueous Zinc-Ion Battery

Noufal Merukan Chola^[a, b] and Rajaram K Nagarale^{*[a, b]}

Self-doping strategy is well-known for enhanced ion transport in electrode materials. Herein we report self-doped thiophene-based conducting polymer (SDTP), where the dopant SO_3^- groups function as the hanging ion carrier mimicking a 'pendulum hand'. It synergistically improves the battery performance, ideally mitigating the dissolution and the enhance ion diffusion kinetics. The diffusion coefficient was determined by three different techniques, i.e., electrochemical impedance spectroscopy (EIS), galvanostatic intermittent titration technique (GITT), and cyclic voltammetry at different sweep rates. The calculated diffusion coefficient for the SDTP was found to be much better than the neat thiophene polymer (NTP). The

material was evaluated as a cathode for an aqueous zinc-ion battery. The specific capacitance of the NTP was found to be 178 mAh g^{-1} at 50 mA g^{-1} current density. It was drastically reduced to 167, 118.2, and 83 mAh g^{-1} after the 5th, 10th, and 30th respective cycles. The polymer SDTP outperformed with a specific capacity of 274, 208, 159, 127, 108 mAh g^{-1} at current densities of 50, 100, 200, 300, 400 mA g^{-1} . It exhibited good rate reversibility, and excellent rate stability with ~99% Coulombic efficiency in an over 4000 continuous cycles at 50 mA g^{-1} suggesting wise molecular engineering is necessary to improve battery performance.

Introduction

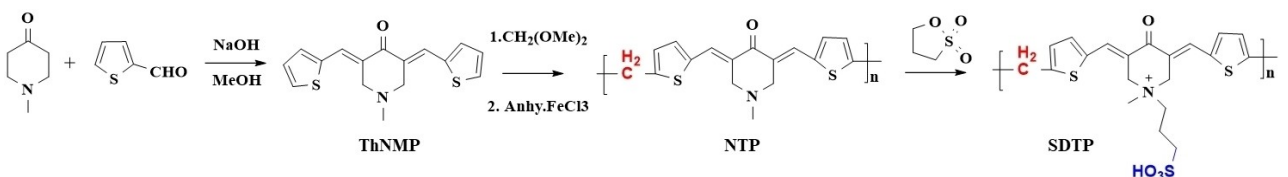
Rechargeable batteries are increasingly getting attention, especially lithium-ion batteries because of their outstanding capacity and energy density. They have been extensively explored to mitigate some of the issues that constrain their practicality, such as using a highly inflammable organic electrolyte, volume expansion over prolonged usage, etc.^[1–6] Therefore, batteries which are user-friendly, compatible with water-based electrolytes, having much better resourcefulness are highly demanding. In recent years many rechargeable batteries have been reported based on various metal ions, such as magnesium, aluminum, potassium, sodium, and zinc in aqueous electrolytes.^[7–11] The zinc-ion-based batteries are very promising because of the abundance of zinc metal, outstanding theoretical capacity due to the two-electron involvement in the charge storage process (819 mAh g^{-1}), and excellent water compatibility (at moderately acidic pH), user and environmental friendliness. They have excellent volumetric and gravimetric energy densities.^[12–14] Unfortunately, the research on aqueous zinc batteries is still unmatured in developing promising cathode materials in particular. Various cathodes have been reported based on the inorganic transition metal oxides,^[15,16] small organic molecules,^[17,18] and organic conducting polymers.^[19] Inorganic materials such as oxides of vanadium

and manganese have been extensively explored as cathodes due to their peculiar layered type lattice structures. Organic molecules are recently getting attention because of their reduced cost, numerous possibilities of diverse molecular engineering, flexibility, abundant resourcefulness, user and environmental friendliness.^[20–22] However, their major disadvantages are reduced electrode stability (the active material gets dislodged into the electrolyte over a prolonged cycling experiment), self-coupling of the transition intermediate, an irreversible structural transformation that causes losing the redox chemistry of the material, and bifacial crystallization on the electrode during charging/discharging experiment.^[23–26] Numerous efforts have been made to address these disadvantages as follows: i) physical encapsulation of the active organic molecules inside the porous structures of appropriate adsorbents such as graphene, graphene oxides, MOFs and COFs,^[27–31] ii) room temperature thermal encapsulation inside carbon nanotubes,^[32,33] iii) cross-linked polymerization of the active organic molecules,^[34] and iv) covalent linkage of the active molecule on polymeric backbone.^[35] In this regard, conducting polymers are a very good choice due to their inherent conducting ability, electrode stability, and relatively large capacity in addition to ease of preparation and reduced cost. PANI,^[36] PEDOT,^[37] polybenzoquinone,^[38] polythiophene,^[39] and polypyrrole,^[40] are some of the conducting polymer-based cathode materials reported as electrode materials. However, they face difficulty in proper ion transport due to the hydrophobicity induced by the polymeric backbone which ultimately worsens the battery performance i.e., low capacity and poor rate performance. The main reason for the poor cycling performance is the deactivation of the polymers caused by deprotonation in electrolytes with low pH. The electrolyte modification for aqueous zinc batteries is troublesome, as commonly used electrolytes are ZnSO_4 or $\text{Zn}(\text{CF}_3\text{SO}_3)_2$ whose

[a] N. M. Chola, Dr. R. K Nagarale
Membrane Science and Separation Technology Division, CSIR-Central Salt and Marine Chemicals Research Institute, Bhavnagar, 364002 Gujarat, India
E-mail: rknagarale@csMRI.res.in

[b] N. M. Chola, Dr. R. K Nagarale
Academy of Scientific and Innovative Research (AcSIR), Ghaziabad-201002, India

 Supporting information for this article is available on the WWW under <https://doi.org/10.1002/batt.202200221>



Scheme 1. Synthetic scheme of the designed cathode. Codes indicated has been used throughout the manuscript.

pH falls in the 4–6.5 range. Several strategies have been developed to address this issue. The functionalization by proton-carrying groups adjacent to the redox center is impressively promising for improved diffusion kinetics. Ying Liu et al reported CNT:PANI:PEDOT: PSS as an integrated cathode for zinc battery which performed much better than the pristine PANI because of the excellently favorable molecular interaction of the aromatic rings via π - π stacking and the sulfonic acid functional groups.^[41] Shi et al introduced sulfonated PANI, as a self-doped conducting polymer, in which SO_3^- groups act as a local proton reservoir that maintains the protonation of the redox center during cycling.^[42] The modified polymer exhibited outstanding cycling stability over 2000 continuous cycles with 70% capacity retention. Covalently attached graphene on self-doped PANI has been reported as a supercapacitor electrode material with excellent cycling stability over 5000 cycles with 100% capacity retention.^[43] Interestingly integrating functional organics as the cathode is a good choice for uninterrupted ion diffusion with much better capacity and rate performance. One such study was reported by group Nan Wang et al., different types of redox functional groups over a single organic scaffold (phenothiazine) nucleus which exhibited 188.24 mAh g⁻¹ with high cycling stability.^[44] Herein, we demonstrate a combined strategy of the above-mentioned concepts by choosing thiophene as the redox active center with hanging sulfonated functional groups. We anticipate that the porous structures as well as the redox active thiophene center of the polymer materials favor each other to gain better cell performance, in addition to the SO_3^- group acting as the local ion reservoir to nullify the ion diffusion path length for Zn^{2+} ions shuttling process. The flexible alkyl group tethered SO_3^- group would act, preferably, charge balancing moiety making a polar ion channel for better ionic diffusion kinetics. Porous structures in the polymer accommodate the ions inside the pores and the anions counterbalance on the redox center during the charging process. And the hanging SO_3^- groups could carry the Zn^{2+} ions acting like the pendulum hand.

Results and Discussion

Material analysis

Monomer and polymer synthesis are shown in Scheme 1. The formation of monomer ThNMP was confirmed by ¹H NMR (CDCl_3). A newly formed vinylic bond was identified by the chemical shift at δ 7.15 ppm. The remaining three aromatic protons on thiophene moiety have been identified at δ 7.93,

7.56, and 7.34 ppm, respectively. Methylene and methyl protons of N-methyl-4-piperidone moiety were located respectively at 3.82 and 2.60 ppm (Figure S1). ¹³C NMR (CDCl_3) chemical shift at δ 185.73 ppm indicated the keto group, signals at δ 127.95, 127.57 ppm referred to the newly formed vinylic carbons. Signals at δ 138.34, 132.71, 130.04, 130.00 ppm corresponded to the aromatic protons on thiophene rings. Two alkyl groups were identified at δ 56.45, and 45.78 ppm for methyl and methylene groups, respectively (Figure S2). Mass analysis was carried out using LCMS (Liquid Chromatography Mass Spectrometry) with a TOF analyzer. The base peak at [M + 1] 302.10 was identified for the product in Figure S3. The single crystal X-ray (ORTEP diagram) was shown in Figure 1, and the crystal data for structure refinement was shown in Table S1. The recorded FTIR spectra are shown in Figures 2(A) and S4(A). Observed peaks were analyzed as 1662.8 cm⁻¹ (strong) for C=O stretching of conjugated ketone, 1602.3 cm⁻¹ (strong) for C=O stretching of α - β unsaturated ketone, 1638.23 cm⁻¹ (strong) for vinylidene C=C bond, 1128.3 cm⁻¹ (strong) due to C=N stretching of a tertiary amine, 965.2 cm⁻¹ for C=C stretching of disubstituted trans-alkene, 860.7 cm⁻¹ (strong) for C=C bending of vinylidene alkene, 1463.2 cm⁻¹ (medium) for methylene C-H bending, 1452 cm⁻¹ for C-H bending of the methyl group. The bands for the thiophene ring were observed at 712.5 cm⁻¹ (out of plane bending), 840 cm⁻¹ (for in-plane bending), and 1081.6 cm⁻¹ for in-plane ring deformation.

The recorded FTIR and XRD for ThNMP were shown in Figure S4(A and B). From the FTIR, typical vinylidene C=C bond, 1128.3 cm⁻¹ (strong) was identified confirming the product formation. Preliminary identification of the crystallinity was noticed by the X-ray analysis.

For NTP, 1662.8 cm⁻¹ (strong) for C=O stretching of conjugated ketone, 1602.3 cm⁻¹ (strong) for C=O stretching of α - β unsaturated ketone, 1638.23 cm⁻¹ (strong) for vinylidene

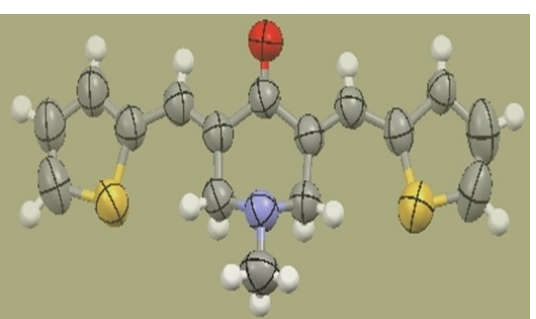


Figure 1. ORTEP diagram of ThNMP. Crystal refinement data were given in Table S1.

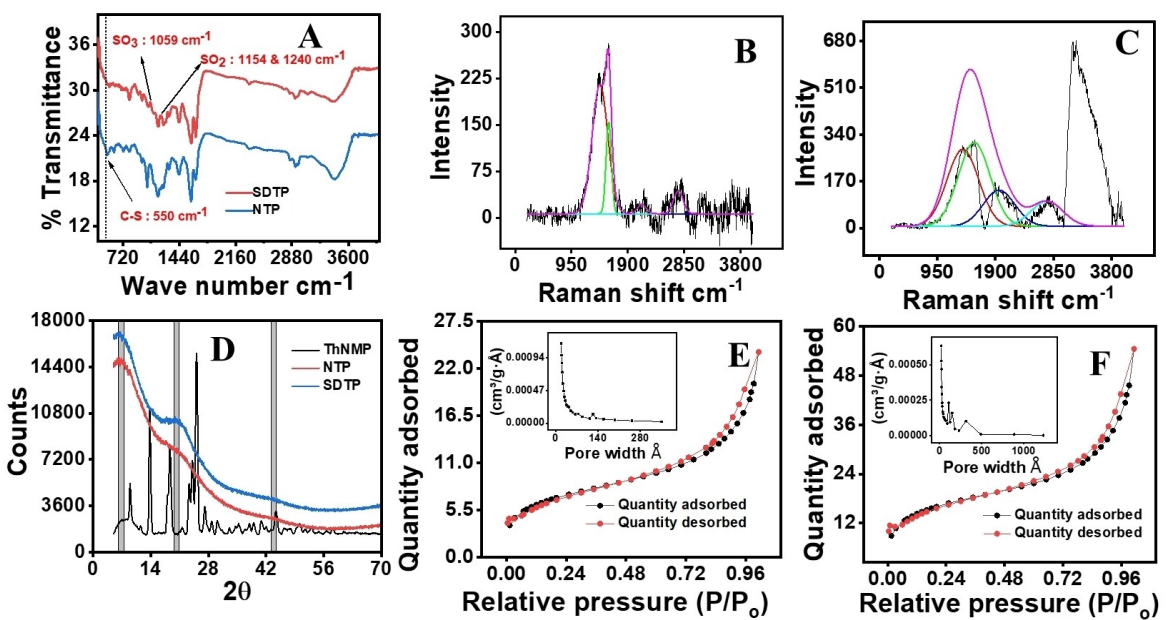


Figure 2. A) FTIR overlay of the NTP&SDTP. Raman spectra for B) NTP and C) SDTP. D) Powder X-ray diffraction pattern of the neat material (ThNMP), corresponding hyperbranched polymer (NTP), and sulfonate introduced polymer (SDTP). BET surface area for E) NTP and F) SDTP, pore volume versus pore width graphs were shown in set.

C=C bond, 1128.3 cm⁻¹ (strong) due to C=N stretching of tertiary amine, 965.2 cm⁻¹ for C=C stretching of disubstituted trans-alkene, 860.7 cm⁻¹ (strong) for C=C bending of vinylidene alkene, 1463.2 cm⁻¹ (medium) for C-H bending methylene group, 550 cm⁻¹ (strong) for C-S stretching frequency, 1452 cm⁻¹ for C-H bending of the methyl group. Following bands were assigned for the thiophene ring, 712.5 cm⁻¹ (out of plane bending), 840 cm⁻¹ (in-plane bending), and 1081.6 cm⁻¹ for in-plane ring deformation. Vibrational frequencies were assigned for the methylene bridge at 1463.2 cm⁻¹ (medium) for C-H bending and 2854 cm⁻¹ (strong) for the C-H stretching of the methylene group. In addition to the characteristic vibrational signals for the NTP, peaks were located at 550 cm⁻¹ for C-S stretching, 1059 for SO₃⁻¹, and 1154 and 1250 cm⁻¹ for SO₂ stretching and bending vibrational frequencies for SDTP, confirming the successful introduction of the tethered sulfonate group.

From the X-ray diffraction pattern, the monomer ThNMP was found to be perfectly crystalline whereas in the case of the knitted polymer (NDT) as well as the self-doped polymer (SDTP) the crystallinity was lost to amorphous nature. Typically, two clear peaks were noticed at 7.2 and 21.7° diffraction angles and a minor broad peak at 43.4. In the case of a self-doped polymer, SDTP, the peaks are found relatively sharp due to a slight gain in the crystallinity compared to the undoped polymer (Figures 2D and S4B). BET surface area analysis was measured for NTP as well as the SDTP, as represented in Figure 2(E and F). The surface area of the polymer after self-doping was found to be 56 cm³ g⁻¹ compared to the neat polymer, which is 24 cm³ g⁻¹. The substantial increment in the surface area of the self-doped polymers is due to the restricted self-aggregation of the oligomers imparted by the intermolecular repulsive interac-

tions. The pore size versus pore width, as shown inset, also confirms the increased porous structures for self-doped polymer (90–320 Å pore diameter) compared to the neat polymers (~70 Å).

Upon Raman spectral analysis two characteristic 'D' and 'G' bands are identified at 1335 and 1612, 2016 and 2749 cm⁻¹ for '2D' and '2D'' bands respectively for NTP. After the introduction of the SO₃ group, the D and G bands were found to be shifted to 1354 cm⁻¹ with 19 cm⁻¹ increments and 1635 cm⁻¹ with an increment of 32 cm⁻¹, in addition to the new '2D' and '2D'' bands identified respectively at 2246 cm⁻¹ and 2871 cm⁻¹. The considerable shift in wavelength for SDTP for the D and G bands was due to the interruption of the close packing alignment of the linear polymer with long-range order due to the repulsive electrostatic interaction after the SO₃⁻¹ group introduction Figure 2(B and C). As the monomer itself contains aromatic rings weak Van der Waals interactions such as π-π stacking between the molecules as well as dipole-dipole and dipole-induced dipole interactions favor the friendly molecular interactions. The Raman spectrum for the neat ThNMP was shown in Figure S5 where characteristics D and G bands were identified at 1404 cm⁻¹ and 1598 cm⁻¹. Various possible molecular alignments have been shown in figure 11. Slight shift in the Raman frequency (compared to the polymer) is due to the nonuniform molecular alignment which has been not found in the polymer NTP, indicating the uniform alignment of the material.^[45–47]

For textural and morphological analysis FESEM imaging was performed. In the case of NTP "twisted rope type" nano-rods with well distinguished fibrous micro rods were observed. Excessive agglomeration of the rods was observed which was substantiated by the TEM images (Figure 3A and B). TEM

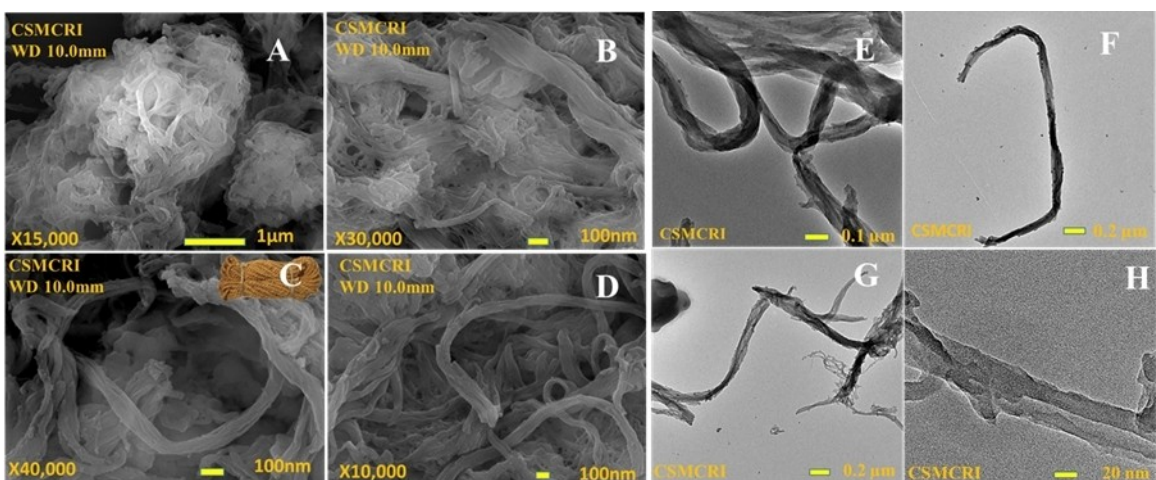


Figure 3. A and B) FESEM images, C and D) HRTEM images of NTP, E and F) FESEM images, G and H) HRTEM images of SDTP. Scale bar: E) 0.1 μ m, F) 0.2 μ m, G) 0.2 μ m, H) 20 nm.

images suggested further the twisted type structural characteristics of the polymers as shown in Figure 3(E and F). In the case of SDTP, the fibrous structure was intact. The aggregation was reduced due to the hanging SO_3^{-1} groups which impart intermolecular repulsive interaction between the fibers (Figure 3C and D). Furthermore, the aromatic thiophene rings impart favorable intermolecular interaction via $\pi-\pi$ stacking, and the H-bonding between the constituent functional groups such as SO_3H , $\text{C}=\text{O}$, tertiary nitrogen, and thiophene sulfur groups. TEM images further confirm the well-ordered structure as shown in Figure 3(G and H). Energy dispersive X-ray spectra of the polymers were represented in Figures S6 and S7, the expected constituent elements were identified as S, N, C suggesting the presence of sulfonic acid in the SDTP polymer, higher sulfur concentration.

Electrochemical analysis

The electrochemical characteristics were initially tested with cyclic voltammetry in 2 M ZnSO_4 solution versus zinc. Reduction and oxidation peaks were observed at 1.17 V and 1.27 V, respectively. Generally, an electrochemical reaction requires a specific time-lapse for the diffusion of the active species towards the electrode surface and the consequent charge transfer of electrons.^[48,49]

With increasing the scan rate the time is restricted for the electrochemical reaction and would limit the required diffusion as well as the charge transfer processes which results in a positive shift for the anodic peak and a negative shift for the cathodic peak. For the neat monomer, ThNMP, peak shift was noticed with a change in scan rate (Figure 4A). The material was stable on the electrode surface. No noticeable decrease in current with multiple cyclic voltammetry (CV) was observed. According to the power law, $i = a\nu^b$ where i is the peak current ν is the sweep rate, and a and b are arbitrary constants, if $b \leq 0.5$ the storage mechanism predominantly follows the diffusion

process, and if $b \geq 0.5$ the mechanism follows non-faradaic surface-confined capacitive mechanism.^[50] Interestingly, it shows a capacitive as well as a diffusive mechanism with a considerably broad area under the CV curve with visible redox peaks. This indicates the pseudocapacitive behavior of the material. Graph of $\log(\text{peak current})$ versus $\log(\text{scan rate})$ gives a straight line with b values of 0.733 and 0.711 for anodic and cathodic peaks, respectively (Figure S8). Since the material showed capacitance behavior, the surface area of the material will directly affect the total capacity. Therefore, we modified the material by polymerization to increase active surface area without compromising the electrochemical behavior of the redox center.

The data revealed that an increase in the surface area of the material results in an increase in specific porosity and capacity of the electrode. However, the redox activity of the material was found to be diminished due to: i) decrease in hydrophilicity of the material after polymerization; ii) sluggish diffusion kinetics, since sulfur atom on thiophene ring shows p-type redox behavior and it follows dual ion shuttling storage mechanism; iii) excessive agglomeration of the material due to the $\pi-\pi$ stacking of the thiophene rings. To overcome these deleterious effects of the electrode material, we functionalize the material with a sulfonate group, which seemingly imparts good hydrophilicity and ion transport. It acts as a local ion reservoir to reduce the diffusion path length of the ions during oxidation/reduction of the redox center. PEDOT:PSS:PANI was reported as an efficient polyaniline-based organic cathode for aqueous zinc-ion batteries.^[51] PEDOT: PSS system hasten the ion diffusion kinetics as well as conductivity by a large number of ionized sulfonate groups on the styrene and conductivity of the PEDOT.^[52] The system, however, works on the weak Van der Waals interactions such as H-bonding, $\pi-\pi$ stacking, dipole-dipole, and dipole-induced dipole interactions.

Sulfonated polyaniline was recently reported as a cathode for zinc battery in which the covalently attached sulfonated group act as the local proton reservoir for facilitating the redox

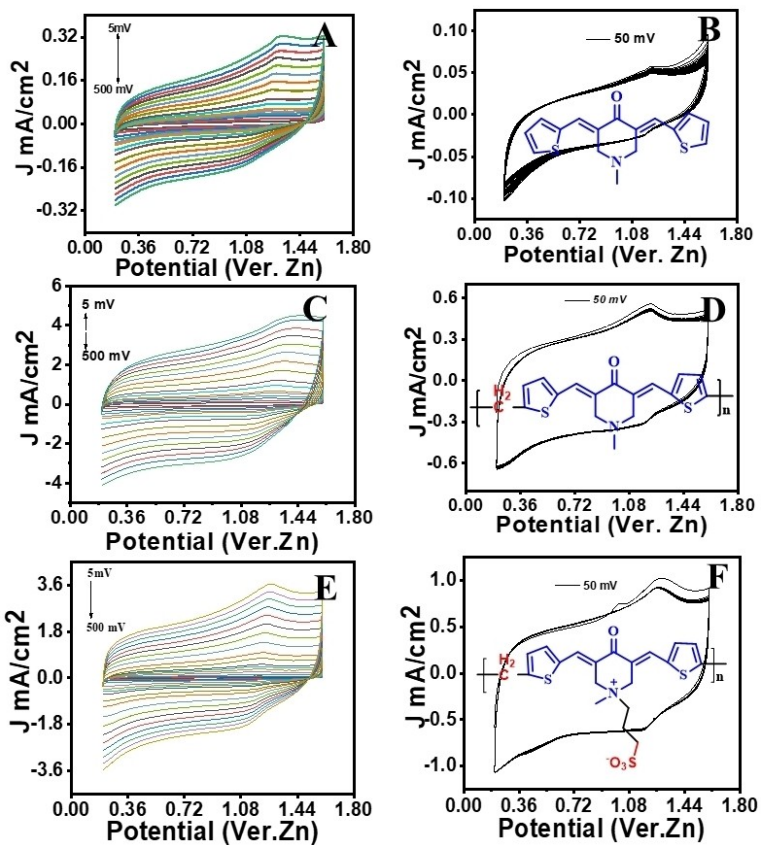


Figure 4. A,C,E) Cyclic voltammogram at different scan rates of ThNMP, NTP and SDTP, respectively. B,D,F) Multiple CV at 50 mV/s for continuous 50 cycles of ThNMP, NTP and SDTP, respectively. (All experiments were performed in 2 M ZnSO₄ solution versus zinc metal as counter and reference electrodes with glassy carbon coated electrode as working electrode).

mechanism of the amine/imine system. Other well-established self-doped systems are PC: PSS,^[53] SPANI,^[54] PSS: PANI,^[55] and conducting polymer integrated with inorganic as well as organic systems (Figure 5).^[56,57] The number of available sulfonate groups, as well as the distance between the redox center and the sulfonate groups, also significantly affects the ion diffusion kinetics which consequently affects the electrochemical performance. We introduced alkyl chain tethered sulfonate functional groups which act as the ‘swinging pendulum hand’ facilitating the ion shuttling between the redox centers. We anticipate that the flexible alkyl chain creates a microchannel for uninterrupted ion shuttling making the diffusion kinetics further faster. From the initial CV analysis, we confirmed that the redox peaks were much more prominent in SDTP compared to NTP polymer. The change in peak potential with the change in scan rate was low (Figure 4E). There was no significant change in peak current in a continuous fifty cycle voltammogram suggesting enhanced electrode stability and a decrease in ohmic resistance (Figure 4B, D and F) by sulfonation of NTP polymer.

To understand the effect of the sulfonyl group introduction on the electrochemical characteristics of the material, we calculated the diffusion coefficient ($D_{Zn^{2+}}$) of Zn²⁺ by three well-known techniques, GITT (Galvanostatic intermittent titration technique), EIS (electrochemical impedance spectroscopy)

and cyclic voltammetry at different sweep rates. From cyclic voltammetry analysis at different sweep rates, $D_{Zn^{2+}}$ was calculated by applying the Randles-Sevcik relation [Equation (1)].^[58,59]

$$I_p = 2.69 \times 10^5 n^{3/2} A D_{Zn^{2+}}^{1/2} C \nu^{1/2} \quad (1)$$

where ' I_p ' indicates the peak current in Ampere, ' n ' is the number of electrons involved in the redox reactions, A is the active surface area of the electrode in cm², $D_{Zn^{2+}}$ is diffusion coefficient of Zn²⁺ ions in cm² s⁻¹, C is the concentration of the Zn²⁺ which is the electrolyte concentration in mol m⁻³ and ν is the sweep rate of the CV in mV s⁻¹. Plotting the peak current versus the square root of sweep rates gives a straight line passing through the origin with a slope equal to $2.69 \times 10^5 n^{3/2} A D_{Zn^{2+}}^{1/2} C$. The diffusion coefficient, $D_{Zn^{2+}}(CV)$, was calculated as 5.401×10^{-6} and 7.206×10^{-6} cm² s⁻¹ respectively for NTP and SDTP. The characteristic diffusivity for SDTP is relatively much higher indicating the influence of the tethered SO₃⁻¹ group on accelerating the ion diffusion kinetics (Figure 6A and B).

EIS is a very useful tool of transient methods to investigate the electrical properties of the electrode surface as well the kinetic aspects as the reaction progresses. Theoretically, EIS is used to understand the physicochemical processes such as

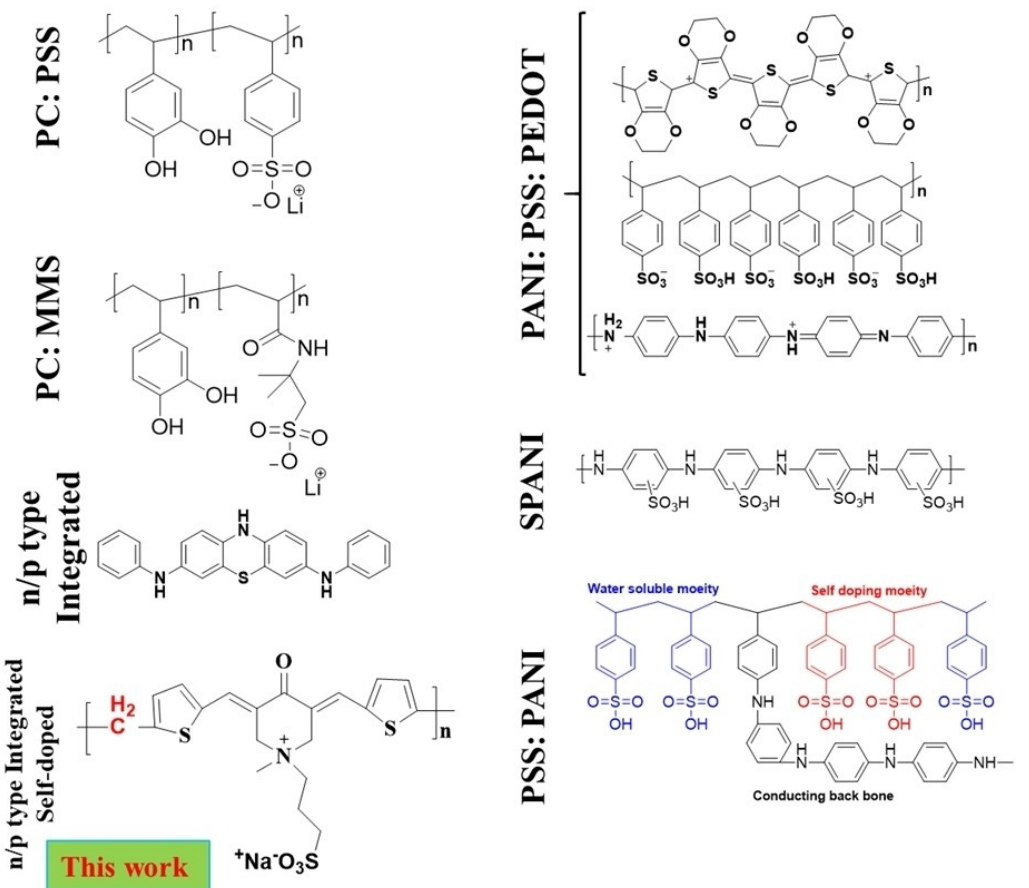


Figure 5. Self-doping strategy of different conducting polymers. Previously reported. PC: polycatechol, MMS: methylmethacrylamide sulfonate, PSS: poly(styrene sulfonate), PEDOT: poly(ethylene dioxy thiophene), SPANI: sulfonated polyaniline.

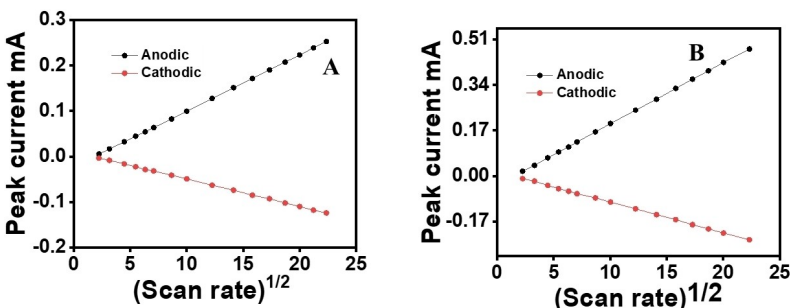


Figure 6. Graphs showing peak current versus square root of scan rate for the Randle Sevcik relation for A) NTP and B) SDTP.

charge transport of electronic and ionic charge carriers and mass transport through diffusion and convection. The high-frequency region depicts the charge transfer control, which appears like a semi-circle, and the low-frequency region gives the idea of the diffusion characteristics which is the Warburg impedance factor that appears as the tangential straight line.^[60]

The EIS analysis was performed using three-electrode systems with platinum and Ag/AgCl as counter and reference electrodes respectively and glassy carbon coated as working electrode. A total volume of 5 μL of the electrode paste was maintained during coating throughout the experiment. Equa-

tion (2) was followed to calculate D_{Zn}^{2+} , where R is the gas constant which is $8.314 \text{ kg m}^2 \text{ S}^{-2} \text{ K}^{-1} \text{ mol}^{-1}$, T is the temperature 298.15 K , D_{Zn}^{2+} is the diffusion coefficient of the Zn^{2+} ions in $\text{cm}^2 \text{ S}^{-1}$, A is the active surface area of the electrode in cm^2 , n is the number electrons involved, F is the Faraday constant $96485.33 \text{ C mol}^{-1}$, C is the concentration of the electrolyte in mol L^{-1} and σ_w slope on the low-frequency region of the Nyquist plot from the EIS analysis which can be obtained from the Equation (3). The Warburg factor was determined from the slope of graph Figure 8(A) which was found to be 4.0625 and $6.701 \Omega \text{ S}^{-1/2}$ respectively for NTP and SDTP, confirming the

higher diffusion contribution from the SO_3^- tethered material. Further $D_{\text{Zn}^{2+}}(\text{EIS})$ was calculated using the Equation (2) as 5.01×10^{-6} and $6.96 \times 10^{-6} \text{ cm}^2 \text{ S}^{-1}$ for NTP and SDTP respectively. The diffusivity of the Zn^{2+} ions for the material with a hanging SO_3^- group was found to be reasonably higher compared to the SO_3^- free material, which judiciously supports the argument on the impact of the tethered SO_3^- group in the diffusion kinetics enhancement. EIS experiments for the two materials at different temperatures have been performed and the results are shown in Figure 7, and the corresponding activation energies (E_a) were calculated as $6.1599 \text{ kJ mol}^{-1}$ for NTP and $33.214 \text{ kJ mol}^{-1}$ for SDTP from the Arrhenius plot as represented in Figure 8(B). This remarkable difference in the E_a also confirmed that the interfacial resistance is much lower in the SO_3^- tethered polymer facilitating uninterrupted ionic as well as an electronic transfer which consequently would be expected to give the improvised capacity performance.

$$D_{\text{Zn}^{2+}}(\text{EIS}) = \frac{R^2 T^2}{2A^2 n^4 F^4 C^2 \sigma_w^2} \quad (2)$$

$$Z_{\text{re}} = R_s + R_{\text{ct}} + \sigma_w \omega^{-1/2} \quad (3)$$

GITT is a unique technique to determine the chemical diffusion coefficient of the charge carrier ions and the equilibrium voltage profile as a function of the state of charge. It has been widely used to determine the mass transport rate

(diffusion coefficient), the reaction rate (relaxation rate), and the composition-dependent activity coefficient in batteries. The technique is based on several underlying assumptions as follows, 1) one-dimensional diffusion of the mobile charge carrier, 2) structural and volume changes of the electrode material are negligible, 3) constant diffusion coefficient during each titration, and 4) the theory follows Fick's law of diffusion.^[61,62] $D_{\text{Zn}^{2+}}(\text{GITT})$ was calculated by following Equation (4), where τ is the constant current pulse time; L is the Zn^{2+} ions diffusion length which is the thickness of the electrode; ΔE_s is the change of steady-state voltage during a single step GITT experiment, ΔE_t is the change in the cell voltage at constant current minus IR loss during each galvanic step.^[63] Charging and discharging potentials were set as 1.6 V and 0.2 V, respectively. Initially, the cell was allowed to be fully charged to 1.6 V and set at resting condition for 30 minutes, then allowed to discharge with 0.1 V fractional increment towards discharge potential of 0.2 V at 5 minutes resting time at each step. The GITT plot for undoped as well as doped material has been shown in figure 9A where the spikes originate from the voltage evolution during the relaxation period. The diffusion coefficient $D_{\text{Zn}^{2+}}(\text{GITT})$ was calculated to be 5.17×10^{-6} and $7.04 \times 10^{-6} \text{ cm}^2 \text{ S}^{-1}$ for NTP and SDTP, respectively.

$$D_{\text{Zn}^{2+}}(\text{GITT}) = \frac{4L^2}{\pi\tau} [\Delta E_s / \Delta E_t]^2 \quad (4)$$

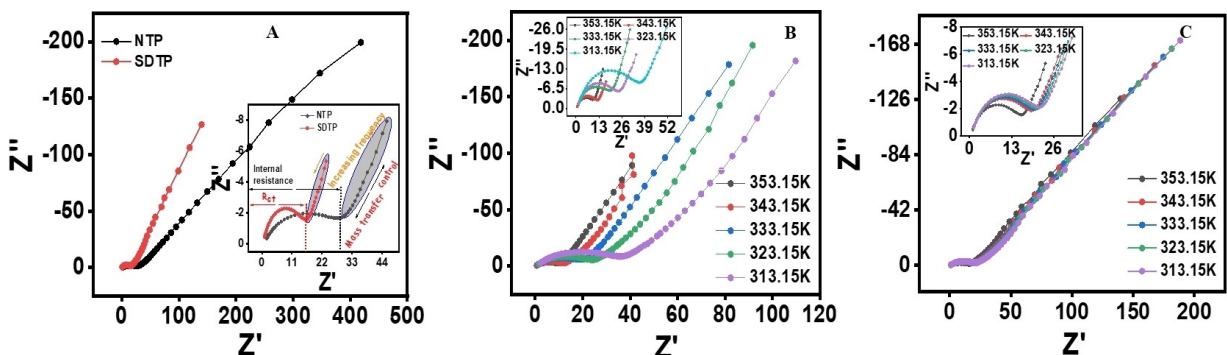


Figure 7. A) Nyquist plot of the NTP and SDTP. B and C) Nyquist plot of NTP and SDTP at different temperatures in kelvin. The experiment was done with a three-electrode setup, a hot plate and thermometer were used for temperature control.

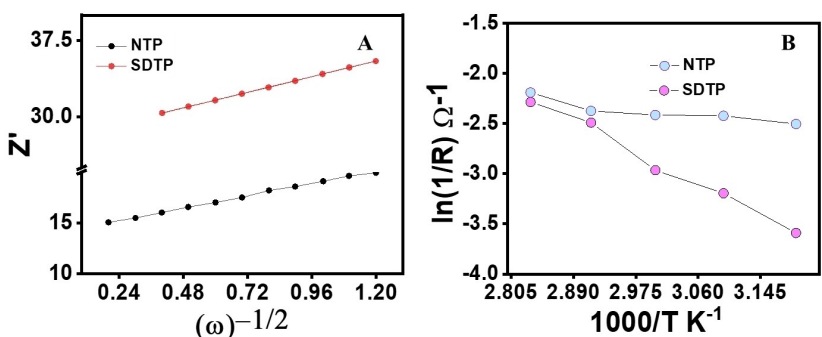


Figure 8. A) Graph showing real impedance versus inverse square root of frequency. B) Arrhenius plot for NTP and SDTP.

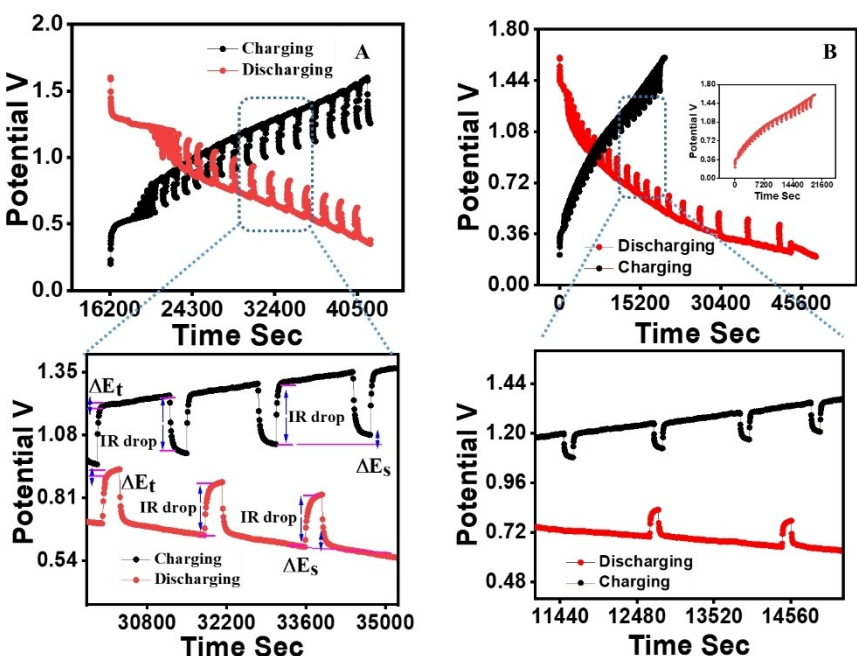


Figure 9. GITT plot for A) NTP and B) SDTP. A constant current was delivered in short pulses, and the system is allowed to relax to equilibrium after each pulse. Parameters in the equation are denoted.

From the GITT titration, it was observed that drastic decrease in charging capacity for NTP compared to the corresponding discharging capacity. During charging, oxidation occurs on the cathode where cation shuttling is essentially crucial for charge balancing as the charge storage follows a dual ion-pairing mechanism, and reduction of the Zn^{2+} ions occurs on the anode. Meanwhile, the discharge process reduction occurs on the cathode where the thiophene redox center, being a p-type organic electrode, accepts electrons that are generated on the anodic counterpart during oxidation. However, the cation shuttling on the cathode during charging/discharging process is more predominantly occurred due to docked sulfonate anion and the excessive porous structures in the polymer.

With self-doped polymers the hanging SO_3^{-1} group can facilitate the accelerated ion diffusion kinetics for SDTP compared to the neat polymer, NTP. Hence, after tethered

SO_3^{-1} group i.e., SDTP, there was a linear change in the GITT graph. With the introduction of sulfonic acid, charging capacity was found to be excellently improved with ~99% Coulombic efficiency, imparted by the greater diffusion kinetics of the anion shuttling Figure 9(B). Impressed with these findings, we further carried out to evaluate the suitability of the material as a cathode in an aqueous zinc ion battery. For the neat ThNMP, we observed 178 mAh g^{-1} at 50 mA g^{-1} , which was drastically reduced to 167, 118.2, and 83 mAh g^{-1} after the 5th, 10th, and 30th cycles as shown in Figure 10(A).

The drastic capacity decay was observed due to the insufficient electrode stability by the dissolution of the material into the electrolyte over a prolonged cycling study. The dissolution was observed by the visual color change of the electrolyte over a long cycling experiment. Figure S9 shows the FESEM images of the cathode after the cycling experiment suggesting a uniform distribution of the electrode material on

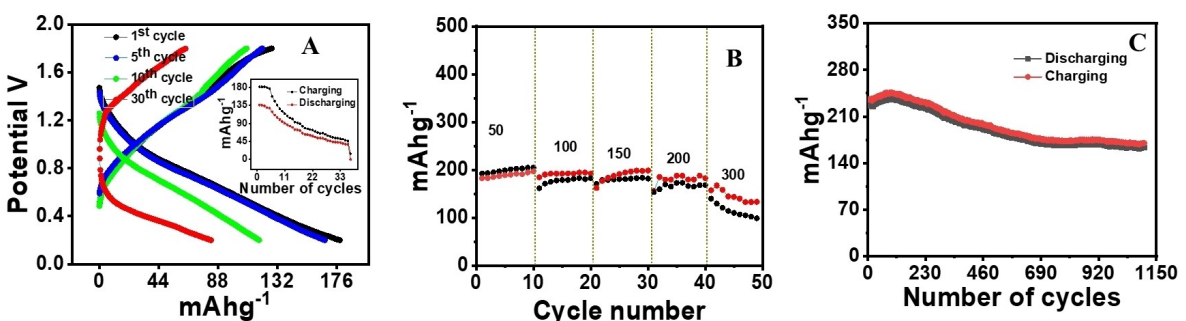


Figure 10. A) Graph showing the charging/discharging cycles of ThNMP, the specific capacitance decay was shown in-set. B) Graph showing rate stability of NTP (the current showed in the graph in mA g^{-1}). C) Cycling stability of the NTP.

the carbon electrode surface. As per our previous report,^[34] we addressed this dissolution issue by converting the molecule into a porous polymer following polymerization in which the monomers are interconnected via a methylene bridge.

Here, the stability of the material was due to the presence of amine and keto group-containing monomer along with two thiophene rings and the tethered SO_3^{-1} groups. They ensure friendly intermolecular interactions and desired structural stability after polymerization as shown in Figure 11. The specific capacity, in the case of NTP, was found to be 193.6 mAh g^{-1} at 50 mA g^{-1} current density which is higher than that of the monomer, due to the non-faradaic surface-confined charge storage mechanism possessed by enlarged surface area after polymerization. The rate performance of the material was evaluated and it was found to be 193.6, 181.1, 172.2, 155.1, and 144 mAh g^{-1} at 50, 100, 150, 200, and 300 mA g^{-1} , respectively (Figure 10B). However, on the long cycling stability test, we

found slow capacity fading after 500 cycles which remained constant until 1000 cycles (Figure 10C).

The deleterious capacity performance at the initial stage was due to the large hydrophobicity of the material in which the ion intercalation was hugely interrupted. It was addressed by the introduction of a sulfonate group tethered by a propyl chain right in the middle of the two electroactive thiophene rings, without hindering the electrochemistry of the parent material. The flexible SO_3^{-1} group can balance the charge, reducing the diffusion path length of the ion migrating from the bulk electrolyte towards the electrode surface. Impressively, it has improved the specific capacitance compared to the neat (ThNMP) as well as the polymer (NTP). The observed specific capacitance of SDTP was 274 mAh g^{-1} at 50 mA g^{-1} and remained at 279.2 mAh g^{-1} after continuous fifty cycles. The material survived the shock of varying current densities with negligible capacity loss as shown in the rate stability test (Figure 12A). The observed specific capacities were 274, 208, 159, 127, 108 mAh g^{-1} at 50, 100, 200, 300, 400 mA g^{-1} , respective current densities. After reverting the current densities to 200 and 100 mA g^{-1} , the observed specific capacities were 152 and 218 mAh g^{-1} , respectively.

The cycling stability was evaluated in 4000 charge/discharge cycles at 50 mA g^{-1} current density. It exhibited an initial specific capacity of 274.2 mAh g^{-1} with 94% capacity retention and ~99% Coulombic efficiency (Figure 12B). The excellent stability of the SDTP was explained based on the specifically porous structural characteristics as well as the hanging SO_3^{-1} groups which facilitate the ion shuttling (Scheme 2). The tethered SO_3^{-1} group would act as the hanging dopant which can carry the Zn^{2+} ions to and fro of the porous structures of the cathode during the cycling process. This is based upon the assumption that the plenty of pores in the polymer act as the local ion reservoir which considerably reduces the diffusion path length of the ions. Since the polymer is highly porous the redox center was not available for the complete participation of the charge storage mechanism. Instead, Zn^{2+} ion insertion-desertion mechanism was predominantly occurring in which the SO_3^{-1} group acts as the local ion carrier.^[64]

Therefore, it is believed that the ion diffusion kinetics was due to the presence of the hanging dopant which is absent in

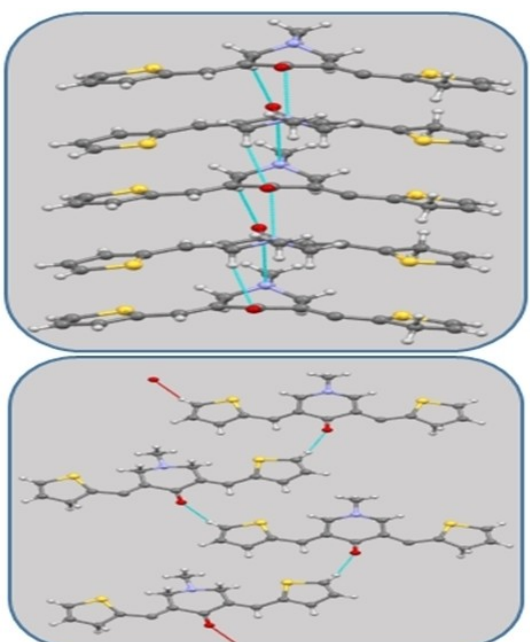


Figure 11. The proposed intermolecular interactions for desired structural stability.

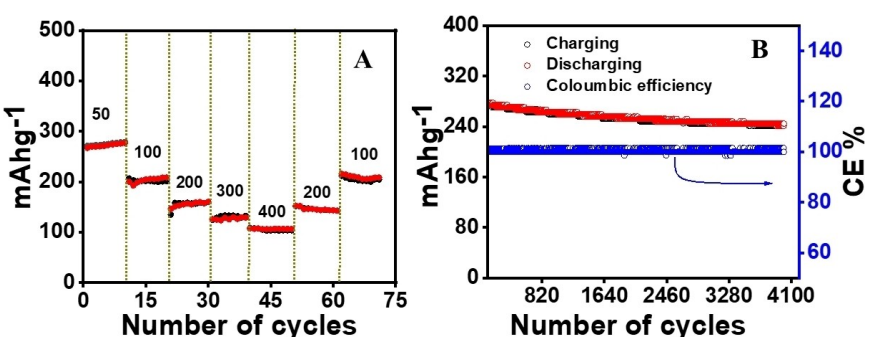
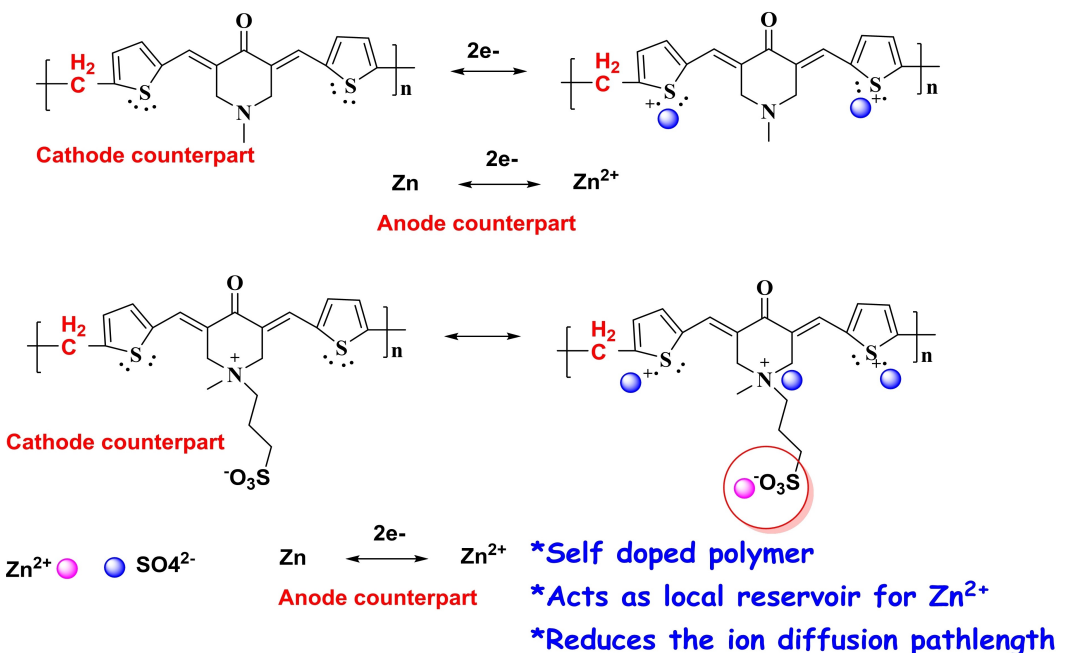


Figure 12. A) Rate stability test of SDTP at different current densities, (the units are in mA g^{-1}). B) Cycling stability test and coulombic efficiency of SDTP over 4000 continuous cycles at 50 mA g^{-1} .



Scheme 2. Illustrates the electrode reactions and charge balancing mechanism.

the case of the undoped (NTP) polymers. It also obvious that the ketonic as well as the other hetero atoms would have substantial influence for the overall enhanced electrochemical performance, imparting good elecrophilicity, much better electrical conductivity due to the extensive conjugation and weak Wan der Vaal interactions such as π - π stacking, ion-dipole interactions.

To enlighten this idea of 'swinging pendulum hand' electrochemical kinetics for the ion diffusion was studied by performing cyclic voltammetry at different sweep rates, following the formalism developed by Laveron.^[65] The kinetic behavior of the modified electrode was analyzed by plotting ΔE versus log (scan rate), where ΔE is the difference between the anodic or cathodic peak potential and the formal potential E° which is obtained from the average of the anodic and cathodic peaks from the voltammogram. The electron transfer coefficient (α) and the electron transfer rate constant (k_s) can be determined by following the Equations (5) and (6), provided the ΔE , i.e., the difference between cathodic and anodic peaks is greater than $200/n$ mV. v_a and v_c are the potential scan rates at the intercept of the straight-line fits to anodic and cathodic data, n is the number of electrons involved during the redox reaction, F is the Faraday's constant ($96,845$ C mole⁻¹), R is the gas constant (8.314 JK⁻¹ mole⁻¹) and T is the temperature which is 298 K.

$$\alpha/(1-\alpha) = v_a/v_c \quad (5)$$

$$k_s = nF\alpha v_c/RT = (1-\alpha)nFv_a/RT \quad (6)$$

The electron transfer coefficient, α , was found to be 0.4744 and 0.4985 respectively for NTP and SDTP. The electron transfer

rate constant, k_s , was determined as 75.11 and 78.85 S⁻¹ for anodic and cathodic peaks respectively for NTP polymer. Whereas for SDTP polymer, the calculated values of k_s for anodic and cathodic peaks were 81.75 S⁻¹ and 81.71 S⁻¹, respectively (Figure 13A and B). At the outset of the initial assessment, for NTP there is a significant difference observed in the k_s value of the anodic and cathodic counterparts due to their sluggish diffusion kinetics. However, in the case of self-doped polymer, SDTP, interestingly k_s values for the anodic and cathodic peaks were more or less same suggesting the negligible ohmic resistance experienced on the electrode during oxidation as well as reduction at respective electrode counterparts. This essentially enhanced the diffusion kinetics of the charge carriers due to the tethered hanging SO₃⁻¹ functional groups. To reaffirm this, $\Delta E/2$ versus log (scan rate) was plotted, as shown in Figure 13(C), where the influence of SO₃⁻¹ group was much clear in which the peak separation was found considerably increasing with scan rate for the NTP polymer. However, for SDTP negligibly small increase in the peak separation was noticed, which is outrightly due to the effect of the hanging SO₃⁻¹ group. Self-aggregation of the particle might be one reason for huge ohmic resistance for neat polymer. The particle size was distributed in the 1452 – 172 nm range, whereas in the case of SDTP the particle size was predominantly 688 nm with no other major size distribution (Figure 13D and E).

This further substantiate the assumption of repulsive interaction of the polymer particles due to the likely charged SO₃⁻¹ groups, which is absent in the case of undoped NTP polymer. Therefore, the outstanding battery performance we observed would be due to the hanging SO₃⁻¹ groups which facilitate the ion shuttling driven by the hanging SO₃⁻¹ group during the redox reaction on the thiophene center. The energy-

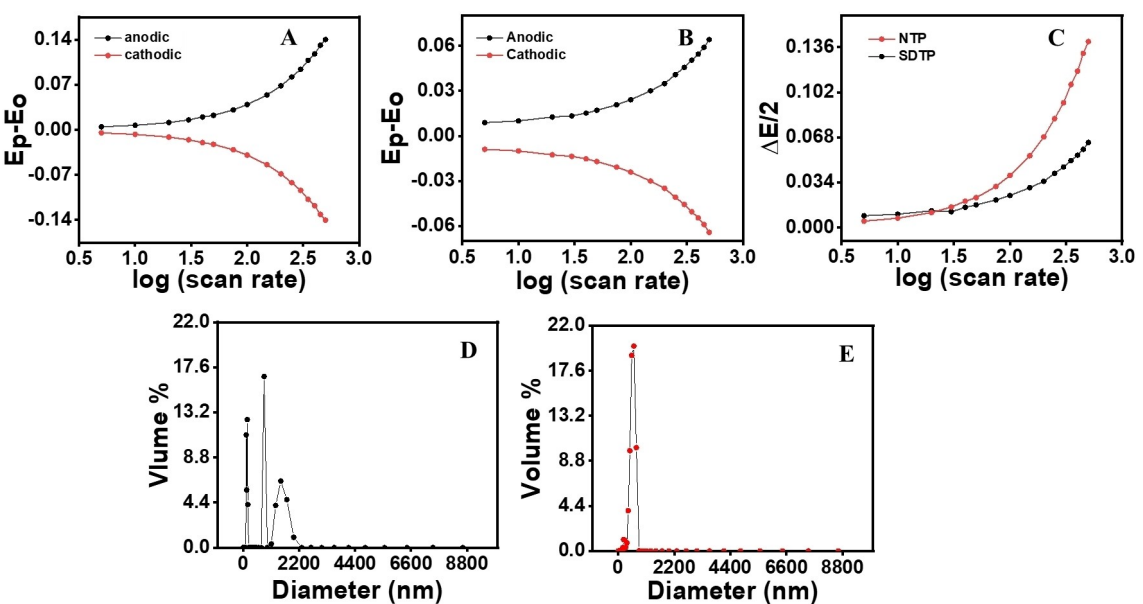


Figure 13. 'Trempet'/Laveron plot for A) NTP and B) SDTP. C) Graph showing the cathodic and anodic peak separation versus $\log(\text{scan rate})$. E_p is the peak current for anodic or cathodic counterpart, E_o is the average of the anodic and cathodic peaks currents following the theory of E. Laveron. The peak potential at different scan rates were obtained from Figure 4. DLS for particle size distribution for D) NTP and E) SDTP.

dispersive X-ray spectroscopy was done for the SDTP coated cathode after the cycling experiment as shown in Figure S10, constituent elements of the cathode material were confirmed. Thiophene moiety is the redox center on the cathode side, which undergoes the p-type redox mechanism providing a single electron in general. A single electron gets released while charging to form a radical soliton. Nevertheless, the redox active center is buried inside the massive polymer matrix the surface confined capacitive storage mechanism predominates. Therefore, Zn^{2+} ions should undergo shuttling from the electrode surface during the charging/discharging process which is predominantly controlled by an electric gradient between the electrode surface and the bulk electrolyte. For NTP, as we assumed, the localized pores with quite a large surface area function as anion reservoirs for counterbalancing during the cycling process. Such localized pores in the polymer matrix act as the reservoir for anions, reducing the diffusion path length of the anions from the bulk electrolyte towards the electrode surface. However, the uncompromising hydrophobicity of the material, in the case of an undoped polymer, hinders the uninterrupted ion shuttling while the cycling progresses suggesting wise molecule design is necessary. Organic molecule containing zinc batteries are increasingly being reported nowadays. Wise molecular designing, numerous choice of diverse molecular engineering, tenability of electrical as well as physical properties are some of the excellent advantages of organic batteries.^[66–68] We have addressed previously the effect of stereochemical ring flipping in organic cathode material on the battery performance, taking quinone polymers as a model, where uncontrolled ring flipping interrupts the ion shuttling during the charging-discharging processes.^[69] This work may give an insightful idea for further research and development in the area of battery research.

Conclusion

We have designed a thiophene-based self-doped knitted polymer as cathode material. To mitigate the dissolution of the electrode material without compromising the ion diffusion kinetics, we integrated the polymerization and self-doping strategies to gain synergistic enhancement in the battery performance. Thiophene rings were flanked on either side of the N-methyl piperidine ring to restore the maximum possible chemical modification. As a small molecule, the ThNMP monomer was found not promising due to the excessive dissolution during the cycling experiment. Its polymer with an interlinked methylene bridge was found to be impressive in addressing the material's hydrophilicity and ion diffusion kinetics. A polymer doped with hanging SO_3 groups which function as the swinging carrier mimicking a 'pendulum hand' synergistically improved the battery performance, ideally mitigating the dissolution and the enhance ion diffusion kinetics. The calculated diffusion coefficient by three different electroanalytical techniques, i.e., EIS, GITT and cyclic voltammetry at different sweep rates were found to be similar. The values were better for SDTP than the undoped polymers. In an aqueous zinc ion battery, as a cathode, the specific capacitance of ThNMP, was found to be 178 mAh g^{-1} at 50 mA g^{-1} current density, which was drastically reduced to 167, 118.2, and 83 mAh g^{-1} after the 5th, 10th, and 30th respective cycles. The SDTP outperformed with a specific capacity of 274, 208, 159, 127, 108 mAh g^{-1} at 50, 100, 200, 300, 400 mA g^{-1} current densities. The material exhibited good rate reversibility, and excellent rate stability with ~99% Coulombic efficiency. Excellent cycling stability was observed over 4000 continuous cycles with 274.2 mAh g^{-1} specific capacity with 94% capacity retention and ~99% Coulombic efficiency. The electron transfer

rate constant, k_s , was determined as 75.11 and 78.85 S^{-1} for anodic and cathodic peaks respectively for NTP polymer. Whereas for SDTP polymer, the calculated values of k_s for anodic and cathodic peaks were 81.75 S^{-1} and 81.71 S^{-1} , respectively. The difference suggested that the tethering group has significant effect on the diffusion of charge carriers which consequently reflects the outperformance in the battery application. With this, we conclude that wise molecular engineering could essentially help to improve battery performance.

Experimental Section

Thiophene-2-carboxaldehyde, dimethoxymethane, and anhydrous FeCl_3 were purchased from Sigma Aldrich. N-methyl-4-piperidone (TCI Chemicals), sodium hydroxide flakes (Central Drug House Pvt. Ltd. New Delhi), 1,3-propanesultone (GLR Innovations New Delhi), ZnSO_4 (Alfa Aesar), Nafion®-117, carbon nanotubes (SRL Pvt. Ltd.), zinc metal plates (Research lab fine-chem industries Mumbai), carbon papers (Spectrum Chemicals) are used for this work. All chemicals were used as such without further purification. Hydrochloric acid, methanol, and acetone were availed from Qualigens.

Material characterization

^1H and ^{13}C NMR spectra were recorded Bruker, Advance II (500 MHz). Mass spectra were obtained by LCMS using the electron impact (EI) ionization method (LC Waters, MS Micromass). FTIR of the sample was studied using FTIR spectra and was recorded with a Perkin-Elmer (Germany) GXFTIR system through the 400–4000 cm^{-1} range. The XRD diffraction patterns of the samples were recorded with a PAN Analytical (Germany) system using the CuK_{α} line ($\lambda=1.5406\text{ \AA}$) through the 5° to 60° range at a scan rate of 10° min^{-1} (well-powdered sample was dried in a vacuum oven at 80°C , kept in a desiccator before the analysis). The surface morphology analysis was done using a JSM-7100F, Japan field emission scanning electron microscope (powdered sample was dispersed in isopropanol, sonicated, and dropped on silicon wafer attached on the copper stub, heated at 60°C , stored in a desiccator before the imaging). BET surface area was analyzed using Micromeritics, ASAP 2010 under N_2 adsorption/desorption at 150°C for four hours (powdery sample was heated to 80°C in a vacuum oven). High-resolution transmission electron microscopy (HRTEM; FEI Tecnai G2 12 Twin) was performed at 120 kV (well-powdered sample was dispersed in isopropanol, sonicated, and dropped on lacey carbon-coated copper grid, vacuum dried in a desiccator before the analysis). Raman analysis was performed using (Model: Alpha, Make: WITec, Germany) in the 400–3000 cm^{-1} frequency range with a 785 nm laser source. UV-Vis absorption spectra were recorded using Shimadzu corp 80109 UV-Vis spectrophotometer using quartz cuvette.

Electrochemical characterization

Carbon paper was heated in conc. HNO_3 for 2 h, washed with DI water and dried. Glassy carbon electrode (GC) was polished in alumina (0.05 micron) slurry, polished using a micron cloth pad, treated with H_2SO_4 , washed with DI water and acetone (*caution! The polishing should be done using a figure 8 motion to avoid grooving the electrode*). Zinc metal plates were treated, initially, with 1 M H_2SO_4 for a few minutes (*metal surface would be corroded for a long time after acid treatment!*), washed with DI water and

acetone, polished with P1200 grit size sandpaper for a shiny surface. CV was performed with a three-electrode set-up, GC as the working electrode, Ag/AgCl , and Platinum as reference and counter electrodes. For the application of zinc battery, zinc metal plates were used as a reference as well as counter electrodes in 2 M ZnSO_4 solution as electrolytes. Galvanostatic charging/discharging was done using a carbon-coated electrode and zinc metal plates, respectively as cathode and anode. *Procedure for electrode coating:* Electro active material, carbon nanotubes and Nafion®-117 were mixed in a mortar pestle (6:3:1 weight ratio), ground well for homogenous powder. The powder mixture was ball milled using an IKA homogenizer (IKA® Ultra Turrax® Tube Drive) and added isopropanol for viscous electrode paste. The paste was drop coated on GC for CV analysis and carbon electrode for cycling experiment. The coated electrode was dried at 60°C overnight before the analysis. CV was performed using CHI 760E Electrochemical Analyzer (CH Instruments, USA) in a potential range of 0–1.6 V. Galvanostatic charging-discharging experiment was performed using a multi-channel battery testing system (Neware-BTS 610). Electrochemical Impedance Spectroscopy (EIS) was performed using a CHI instrument with three electrodes set up in a frequency range of 0.1–200 MHz with an amplitude of 5 mV.

Preparation of monomer (ThNMP)

N-methyl-4-piperidone (3 mL, 23.8 mmol) was added to the stirring solution of thiophene-2-carboxaldehyde (4.5 mL, 48.16 mmol) in 30 mL methanol in the round bottom flask. Sodium hydroxide flakes (2 g, 50 mmol) were dissolved in minimum methanol and added slowly into the reaction mixture allowing for vigorous stirring for initial 15 minutes. The reaction mixture was refluxed for 2 hours resulting in the yellow-colored reaction mixture, completion of the reaction was confirmed by TLC. The reaction mixture was cooled and poured into crushed ice, the yellow-colored precipitate was filtered washed with water, and recrystallized from dichloromethane (95%). Molecular structure was confirmed by NMR (1H, 13C), HRMS-TOF, and FTIR analysis. ^1H NMR (600 MHz): δ 7.93 (s, 1H), 7.56 (d, $J=5.1\text{ Hz}$, 1H), 7.34 (d, $J=3.5\text{ Hz}$, 1H), 7.26 (solvent peak), 7.15 (dd, $J=5.0, 3.8\text{ Hz}$, 1H), 3.82 (d, $J=1.4\text{ Hz}$, 2H), 2.60 (s, 3H). ^{13}C NMR (600 MHz) δ 185.73, 138.34, 132.71, 130.04, 130.00, 127.95, 127.57, 56.45, 45.78. ESI-Mass [M+1] 302.10, single crystal structure has been solved. Deposition Number(s) 2182194 (for ThNMP) contain(s) the supplementary crystallographic data for this paper. These data are provided free of charge by the joint Cambridge Crystallographic Data Centre and Fachinformationszentrum Karlsruhe Access Structures service.

Polymerization (NTP)

The product ThNMP (2 g, 9.6 mmol) was dissolved in 30 mL anhydrous DCE, added Dimethoxymethane (1.7 mL, 18.9 mmol) allowed to stir for 5 minutes for a homogenous solution. The solution was purged by N_2 for 15 minutes, added anhydrous FeCl_3 , stirred for 1 hour, and heated to reflux for 24 hours. Slight formation of Black product was observed at initial 5–6 hours reflux. The reaction mixture was cooled, filtered the product as black powder, and washed with DCE, methanol, and DI water several times. The product was boiled in methanol for 24 hours to wash out the low molecular weight soluble oligomers. It was finally washed with acetone and plenty of DI water, vacuum dried (89%), (the product was found insoluble in most of the common solvents). Characterization was done by FTIR and Raman spectral analysis.

Preparation of self-doped polymer (SDTP)

The product ThNMP-COF (1 g, 3.1 mmol) was stirred in 20 mL methanol and added 1,3-propanesultone (excess, 0.5 mL) to the stirring solution. The reaction mixture was kept for 24 hours with vigorous stirring, the black product was filtered, washed with methanol, DI water and vacuum dried (85%). Characterization was done by FTIR and Raman spectral analysis.

Acknowledgements

Director, CSIR-CSMCRI is acknowledged for his tremendous support and inspiration. The divisional chair of the MSST department and analytical & instrumentation facility of CSMCRI-CSIR Bhavnagar is also greatly acknowledged. Dr. Srinu Tothadi, scientist at CSMCRI is acknowledged for molecular modeling based on crystal data. R.K.N. thanks for the financial support, grant no. DST/TMD/MES/2K18/194(G) from Technology Mission Division, Energy and Water. CSIR-CSMCRI manuscript number 84/2022.

Conflict of Interest

The authors declare no conflict of interest.

Data Availability Statement

The data that support the findings of this study are available from the corresponding author upon reasonable request.

Keywords: aqueous electrolyte • conducting polymer • polythiophene • self-doping • zinc-based storage device

- [1] A. Manthiram, *J. Phys. Chem. Lett.* **2011**, *2*, 176–184.
- [2] J. B. Goodenough, *Nat. Electron.* **2018**, *1*, 204–204.
- [3] J. B. Goodenough, *Energy Environ. Sci.* **2014**, *7*, 14–18.
- [4] J. B. Goodenough, Y. Kim, *J. Power Sources* **2011**, *196*, 6688–6694.
- [5] M. Armand, J. M. Tarascon, *Nature* **2008**, *451*, 652–657.
- [6] A. Manthiram, *Nat. Commun.* **2020**, *11*, 1550.
- [7] G. Fang, J. Zhou, A. Pan, S. Liang, *ACS Energy Lett.* **2018**, *3*, 2480–2501.
- [8] M. Li, J. Lu, X. Ji, Y. Li, Y. Shao, Z. Chen, C. Zhong, K. Amine, *Nat. Rev. Mater.* **2020**, *5*, 276–294.
- [9] Y. Liang, H. Dong, D. Aurbach, Y. Yao, *Nat. Energy* **2020**, *5*, 646–656.
- [10] S. K. Das, S. Mahapatra, H. Lahan, *J. Mater. Chem. A* **2017**, *5*, 6347–6367.
- [11] H. Wang, D. Yu, C. Kuang, L. Cheng, W. Li, X. Feng, Z. Zhang, X. Zhang, Y. Zhang, *Chem* **2019**, *5*, 313–338.
- [12] Y. Shi, Y. Chen, L. Shi, K. Wang, B. Wang, L. Li, Y. Ma, Y. Li, Z. Sun, W. Ali, S. Ding, *Small* **2020**, *16*, 2000730.
- [13] W. Shang, W. Yu, Y. Liu, R. Li, Y. Dai, C. Cheng, P. Tan, M. Ni, *Energy Storage Mater.* **2020**, *31*, 44–57.
- [14] L. E. Blanc, D. Kundu, L. F. Nazar, *Joule* **2020**, *4*, 771–799.
- [15] X. Gao, H. Zhang, X. Liu, X. Lu, *Carbon Energy* **2020**, *2*, 387–407.
- [16] L. Wang, K. W. Huang, J. Chen, J. Zheng, *Sci. Adv.* **2019**, *5*, eaax4279.
- [17] C. Fribe, A. Lex Balducci, U. S. Schubert, *ChemSusChem* **2019**, *12*, 4093–4115.
- [18] T. B. Schon, B. T. McAllister, P. F. Li, D. S. Seferos, *Chem. Soc. Rev.* **2016**, *45*, 6345–6404.
- [19] X. Zang, X. Wang, H. Liu, X. Ma, W. Wang, J. Ji, J. Chen, R. Li, M. Xue, *ACS Appl. Mater. Interfaces* **2020**, *12*, 9347–9354.
- [20] H. Kim, J. E. Kwon, B. Lee, J. Hong, M. Lee, S. Y. Park, K. Kang, *Chem. Mater.* **2015**, *27*, 7258–7264.
- [21] A. Mauger, C. Julien, A. Paolella, M. Armand, K. Zaghib, *Materials* **2019**, *12*, 1770.
- [22] H. Ye, Y. Li, *Energy Fuels* **2021**, *35*, 7624–7636.
- [23] D. Kundu, P. Oberholzer, C. Glaros, A. Bouzid, E. Tervoort, A. Pasquarello, M. Niederberger, *Chem. Mater.* **2018**, *30*, 3874–3881.
- [24] Q. Zhao, W. Huang, Z. Luo, L. Liu, Y. Lu, Y. Li, L. Li, J. Hu, H. Ma, J. Chen, *Sci. Adv.* **2018**, *4*, eaao1761.
- [25] R. L. Belanger, B. Commarieu, A. Paolella, J.-C. Daigle, S. Bessette, A. Vlijh, J. P. Claverie, K. Zaghib, *Sci. Rep.* **2019**, *9*, 1213.
- [26] Q. Ren, Y. Yuan, S. Wang, *ACS Appl. Mater. Interfaces* **2022**, *14*, 20, 23022–23032.
- [27] S. Flandois, B. Simon, *Carbon* **1999**, *37*, 165–180.
- [28] A. E. Baumann, D. A. Burns, B. Liu, V. S. Thoi, *Chem. Commun.* **2019**, *2*, 86.
- [29] R. Zhao, Z. Liang, R. Zou, Q. Xu, *Joule* **2018**, *2*, 2235–2259.
- [30] G. Wang, M. Yu, X. Feng, *Chem. Soc. Rev.* **2021**, *50*, 2388–2443.
- [31] N. M. Chola, R. K. Nagarale, *J. Electrochem. Soc.* **2020**, *167*, 100552.
- [32] N. M. Chola, V. Singh, V. Verma, R. K. Nagarale, *J. Electrochem. Soc.* **2022**, *169*, 020503.
- [33] N. M. Chola, R. K. Nagarale, *Mater. Adv.* **2022**, *3*, 4310–4321.
- [34] N. M. Chola, R. K. Nagarale, *J. Electrochem. Soc.* **2021**, *168*, 100501.
- [35] M. Kolek, F. Otteny, J. Becking, M. Winter, B. Esser, P. Bieker, *Chem. Mater.* **2018**, *30*, 6307–6317.
- [36] H. Y. Shi, Y.-J. Ye, K. Liu, Y. Song, X. Sun, *Angew. Chem. Int. Ed.* **2018**, *57*, 16359–16363; *Angew. Chem.* **2018**, *130*, 16597–16601.
- [37] D. Bin, W. Huo, Y. Yuan, J. Huang, Y. Liu, Y. Zhang, F. Dong, Y. Wang, Y. Xia, *Chem* **2020**, *6*, 968–984.
- [38] C. Guo, Y. Liu, L. Wang, D. Kong, J. Wang, *ACS Sustainable Chem. Eng.* **2022**, *10*, 213–223.
- [39] J. Xiao, X. Jia, C. Duan, F. Huang, H. Yip, Y. Cao, *Adv. Mater.* **2021**, *33*, 2008158.
- [40] Y. Zhang, G. Xu, X. Liu, X. Wei, J. Cao, L. Yang, *ChemElectroChem* **2020**, *7*, 2762–2770.
- [41] Y. Liu, L. Xie, W. Zhang, Z. Dai, W. Wei, S. Luo, X. Chen, W. Chen, F. Rao, L. Wang, Y. Huang, *ACS Appl. Mater. Interfaces* **2019**, *11*, 30943–30952.
- [42] H. Y. Shi, Y.-J. Ye, K. Liu, Y. Song, X. Sun, *Angew. Chem. Int. Ed.* **2018**, *57*, 16359–16363; *Angew. Chem.* **2018**, *130*, 16597–16601.
- [43] C. Y. Kung, T.-L. Wang, H.-Y. Lin, C.-H. Yang, *J. Power Sources* **2021**, *490*, 229538.
- [44] N. Wang, Z. Guo, Z. Ni, J. Xu, X. Qiu, J. Ma, P. Wei, Y. Wang, *Angew. Chem. Int. Ed.* **2021**, *60*, 20826–20832.
- [45] K. N. Kudin, B. Ozbas, H. C. Schniepp, R. K. Prud'homme, I. A. Aksay, R. Car, *Nano Lett.* **2008**, *8*, 36–41.
- [46] A. C. Ferrari, D. M. Basko, *Nat. Nanotechnol.* **2013**, *8*, 235–246.
- [47] K. I. Hadjiiivanov, D. A. Panayotov, M. Y. Miyahaylov, E. Z. Ivanova, K. K. Chakarov, S. M. Andonova, N. L. Drenchev, *Chem. Rev.* **2021**, *121*, 1286–1424.
- [48] K. J. Aoki, J. Chen, Y. Liu, B. Jia, *J. Electroanal. Chem.* **2020**, *856*, 113609.
- [49] E. M. Espinoza, J. A. Clark, J. Soliman, J. B. Derr, M. Morales, V. I. Vullev, *J. Electrochem. Soc.* **2019**, *166*, H3175–H3187.
- [50] T. Brousse, D. Bélanger, J. W. Long, *J. Electrochem. Soc.* **2015**, *162*, A5185–A5189.
- [51] Y. Liu, L. Xie, W. Zhang, Z. Dai, W. Wei, S. Luo, X. Chen, W. Chen, F. Rao, L. Wang, Y. Huang, *ACS Appl. Mater. Interfaces* **2019**, *11*, 30943–30952.
- [52] P. R. Das, L. Komsisyska, O. Ostros, G. Wittstock, *J. Electrochem. Soc.* **2015**, *162*, A674–A678.
- [53] D. Chhin, L. Padilla-Sampson, J. Malenfant, V. Rigaut, A. Nazemi, S. B. Schougaard, *ACS Appl. Energ. Mater.* **2019**, *2*, 7781–7790.
- [54] Y. Wang, H. Jiang, R. Zheng, J. Pan, J. Niu, X. Zou, C. Jia, *J. Mater. Chem. A* **2020**, *8*, 12799–12809.
- [55] M.-R. Choi, S.-H. Woo, T.-H. Han, K.-G. Lim, S.-Y. Min, W. M. Yun, O. K. Kwon, C. E. Park, K.-D. Kim, H.-K. Shin, M.-S. Kim, T. Noh, J. H. Park, K.-H. Shin, J. Jang, T.-W. Lee, *ChemSusChem* **2011**, *4*, 363–368.
- [56] V. A. Nguyen, C. Kuss, *J. Electrochem. Soc.* **2020**, *167*, 065501.
- [57] X. Hong, Y. Liu, Y. Li, X. Wang, J. Fu, X. Wang, *Polymer* **2020**, *12*, 331.
- [58] R. K. Nagarale, J. M. Lee, W. Shin, *Electrochim. Acta* **2009**, *54*, 6508–6514.
- [59] N. M. Chola, S. Sreenath, B. Dave, R. K. Nagarale, *Electrophoresis* **2019**, *40*, 2979–2987.
- [60] W. Weppner, R. A. Huggins, *J. Electrochem. Soc.* **1977**, *124*, 1569.
- [61] D. W. Dees, S. Kawauchi, D. P. Abraham, J. Prakash, *J. Power Sources* **2009**, *189*, 263–268.
- [62] B. A. Mei, O. Munteşari, J. Lau, B. Dunn, L. Pilon, *J. Phys. Chem. C* **2018**, *122*, 194–206.

- [63] A. Verma, K. Smith, S. Santhanagopalan, D. Abraham, K. P. Yao, P. P. Mukherjee, *J. Electrochem. Soc.* **2017**, *164*, A3380–A3392.
- [64] L. Zhu, Y. Shen, M. Sun, J. Qian, Y. Cao, X. Ai, H. Yang, *Chem. Commun.* **2013**, *49*, 11370.
- [65] E. Laviron, *J. Electroanal. Chem. Interfacial Electrochem.* **1979**, *101*, 19–28.
- [66] S. Xu, M. Sun, Q. Wang, C. Wang, *J. Semicond.* **2020**, *41*, 091704.
- [67] Y. Chen, J. Li, Q. Zhu, K. Fan, Y. Cao, G. Zhang, C. Zhang, Y. Gao, J. Zou, T. Zhai, C. Wang, *Angew. Chem. Int. Ed.* **2022**, e202116289.
- [68] H. Cui, L. Ma, Z. Huang, Z. Chen, C. Zhi, *SmartMat.* **2022**, 1–17.
- [69] N. M. Chola, R. K. Nagarale, *J. Electrochem. Soc.* **2022**, *169*, 040534.

Manuscript received: May 16, 2022
Revised manuscript received: August 12, 2022
Accepted manuscript online: August 12, 2022
Version of record online: August 31, 2022